Monolithic Millimeter-Wave Two-Dimensional Horn Imaging Arrays

GABRIEL M. REBEIZ, MEMBER, IEEE, DAYALAN P. KASILINGAM, MEMBER, IEEE, YONG GUO, PHILIP A. STIMSON, AND DAVID B. RUTLEDGE, SENIOR MEMBER, IEEE

Abstract—**A monolithic two-dimensional horn imaging array has been fabricated for millimeter wavelengths. In this configuration, a dipole is suspended in an etched pyramidal cavity on a 1-μm silicon-oxynitride membrane. This approach leaves room for low-frequency connections and processing electronics. The theoretical pattern is calculated by approximating the horn structure by a cascade of rectangular-waveguide sections. The boundary conditions are matched at each of the waveguide sections, and at the aperture of the horn. Patterns at 93 and 242 GHz agree well with theory. Horn aperture efficiencies of 44 ± 4%, including mismatch and resistive losses, have been measured. A detailed breakdown of the losses is presented in the paper. The coupling efficiency to various f-number imaging systems is investigated, and a coupling efficiency of 24% for an $f \setminus 0.7$ imaging system, including spillover, taper, mismatch and resistive losses, has been measured. Possible application areas include imaging arrays for remote sensing, plasma diagnostics, radiometry and superconducting tunnel-junction receivers for radio astronomy.**

I. INTRODUCTION

MILLIMETER-WAVE imaging systems are becoming important in many scientific and military applications [1]–[5]. They provide better resolution than microwave imaging systems and are less affected by atmospheric conditions than infrared systems. The use of a single detector in a mechanically scanned imaging system is a well-established technique for millimeter and submillimeter-wave imaging [1], [2]. However, these scanning systems, whether electronic or mechanical, are inadequate in many applications. The events may be too fast, or the required integration time too long. The way to circumvent this limitation is to image all points simultaneously onto multiple sensors. A millimeter-wave imaging array consists of a large number of antennas with detectors, placed at the focal plane of an imaging system (Fig. 1). The antennas are the feeds for lenses and reflectors in the focusing optics, and the outputs from all the detectors make up the image. A monolithic focal-plane imaging array is an attractive solution for an imaging array. In these systems, the antennas and detectors are integrated on dielectric substrates such as quartz, silicon and gallium arsenide [6], [7].

Antennas on dielectric substrates suffer from losses to substrate modes [8]. Researchers have attacked this problem in several different ways. Twin-slot [9] and twin-dipole [10] designs reduce the substrate mode power and improve the patterns at the same time. Tapered-slot antennas use the substrate mode on a relatively thin substrate effectively to control the shape of the beam [11]. A lens is often mounted on the back of the substrate to eliminate the substrate modes [6]–[8], at the expense of relatively poor patterns [12] and dielectric absorption losses, which may be severe at submillimeter wavelengths [13]. Recently, however, log-periodic and spiral antennas have shown good patterns with a quartz substrate lens [14], and a two-element Yagi antenna has been successfully demonstrated on a TPX lens [15]. Another way to solve the substrate problem is to integrate the antennas on silicon-oxynitride membranes less than a micron thick. This thickness is so small compared to a wavelength that the antenna effectively radiates in free space. This eliminates the substrate modes and the substrate lens, and allows the use of free-space antenna designs and techniques [16].

Monolithic millimeter-wave imaging arrays have previously been limited to one-dimensional designs, although Yngvesson [11], [17] has made two-dimensional arrays by stacking linear arrays of tapered slot antennas. One problem in two-dimensional arrays is that for efficient reception, the effective area of the antenna must be comparable to the area of the resolution cell, but at the same time there has to be room for electronics and connections. We approach ths problem by fabricating a two-dimensional array of pyramidal horns etched in silicon (Figs. 2, 3). Inside each horn is a probe antenna suspended on a 1-μm thick silicon-oxynitride membrane. The horn collects the energy incident on a resolution cell, and focuses it to the probe antenna on the membrane. All of the probe dipoles, detectors and interconnections are integrated on the same silicon wafer. A major advantage of this approach is that the probe antennas are much smaller than a unit cell; typically the membrane occupies less than 25% of the wafer surface, and the rest of the wafer is available for connections and electronics. The dielectric absorption losses are eliminated and the design can easily be scaled for different wavelengths.

Manuscript received June 16, 1988; revised May 18, 1989. This work was supported by the Army Research Office, the Department of Energy, the Innovative Space Technology Center at the Jet Propulsion Laboratory, the Innovative Science and Technology Program of the Strategic Defense Initiative Organization, and Aerojet Electrosystems.

G. M. Rebeiz was with the Division of Engineering and Applied Science, California Institute of Technology, Pasadena CA. He is now with the Electrical Engineering and Computer Science Department, University of Michigan, Ann Arbor, MI 48109-2122.

D. P. Kasilingam was with the Division of Engineering and Applied Science, California Institute of Technology, Pasadena, CA. He is now with Ocean Research and Engineering, La Canãda, CA 91011.

Y. Guo, P. A. Stimson, and D. B. Rutledge are with the Division of Engineering and Applied Science, California Institute of Technology, Pasadena, CA 91125.

IEEE Log Number 9036712.

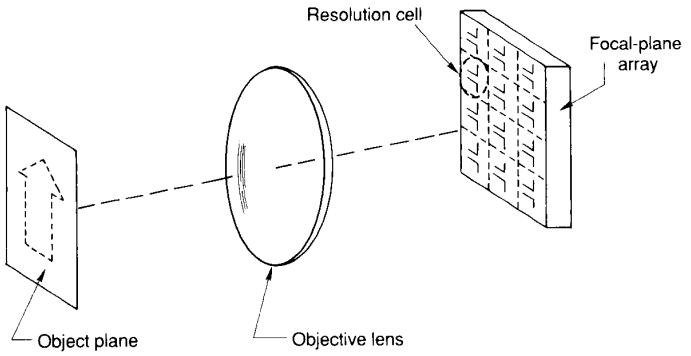

Fig. 1. Perspective view of a two-dimensional horn imaging array.

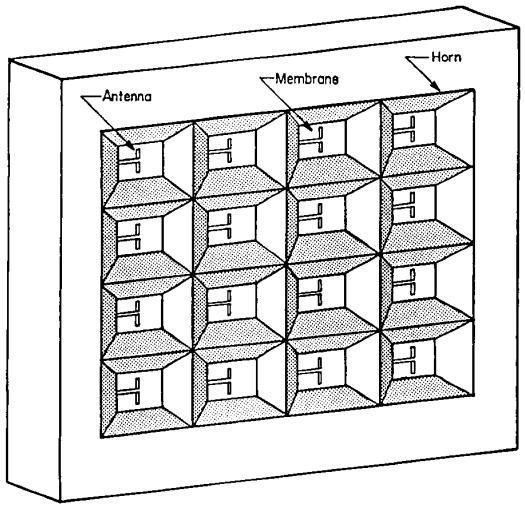

Fig. 2. Millimeter-wave imaging system with a focal-plane imaging array.

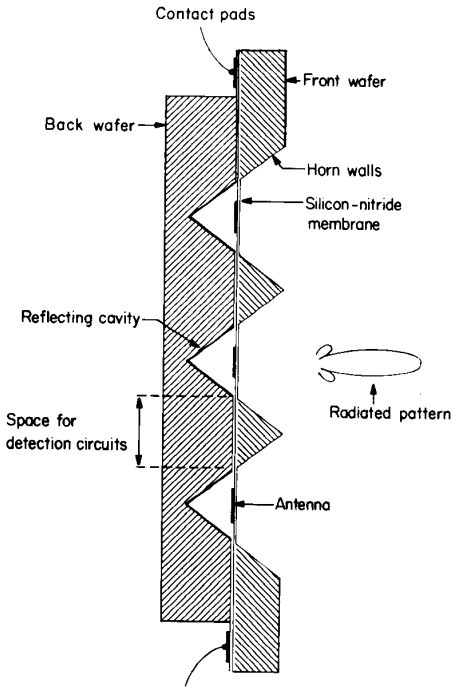

Fig. 3. Side view of a horn array. The 242-GHz array is a two-wafer stack, as shown here. It is also possible to stack more wafers; the 93-GHz array has four wafers. The probe antenna is integrated onto the membrane.

II. Fabrication

The horn array is a stacked silicon-wafer structure (Fig. 3). The back wafer acts as a reflecting cavity, while the front wafer acts as the mouth of the horn. The openings on the front wafer determine the aperture size of the horn antennas. The thickness of the front wafer determines the position of the probe antennas inside the pyramidal horns. The opening on the back wafer is made equal to the size of the membrane, to result in a pyramidal horn with smooth sidewalls.

The horns are made by anisotropic etching of silicon in an ethylenediamine-pyrocatechol solution [18]. This widely used etchant naturally forms pyramidal holes bounded by ⟨111⟩ crystal planes in ⟨100⟩ silicon. The flare angle of the horn is fixed by the orientation of the crystal planes at 70.6°, which is larger than desirable. It may be possible to achieve smaller flare angles with ion-beam milling or reactive-ion etching. It is also necessary to align the mask openings to the ⟨110⟩ crystal planes, because a misalignment increases the size of the etched pyramidal cavity. To produce the membrane, a silicon oxynitride layer is deposited on the front wafer using plasma enhanced chemical vapor deposition [19], and the silicon etched away to leave the free standing membrane. The layer must be in tension to yield flat, rigid membranes. Details of this process are available in [20].

After etching, the probe antennas, detectors, and connections are fabricated by standard photolithographic techniques. The horn sidewalls are coated with gold to reduce the resistive losses. The probe antennas are made of silver 1000 Å thick. The detectors are 4 μm-square bismuth microbolometers [21] with a dc resistance of 140 Ω, and a dc responsivity of 10 V/W at a bias of 100 mV. It should also be possible to make superconducting tunnel junctions on the membranes. The wafer stack is made by aligning the wafers in a mask aligner, and gluing them with photoresist spread around the corners. A completed horn is shown in Fig. 4. There is typically a 20 μm step in the pyramidal-cavity sidewalls when any two wafers are joined together. This is due to a

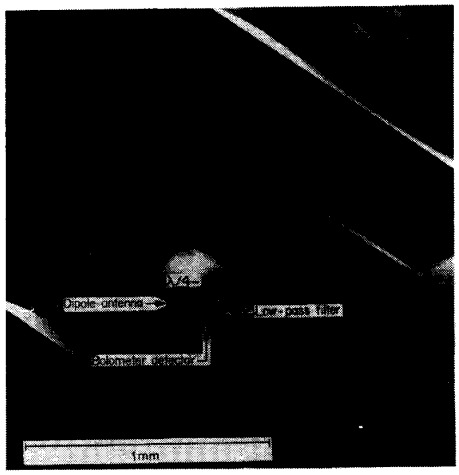

Fig. 4. A scanning electron micrograph of a finished horn element for 242 GHz. The misalignment between the wafers is 20 μm.

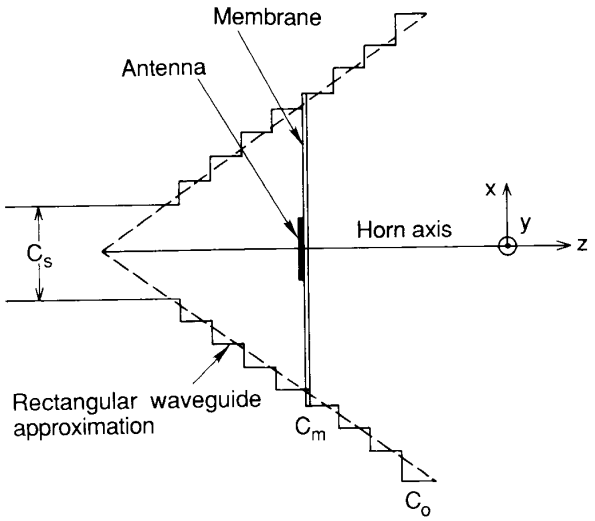

Fig. 5. A stepped waveguide approximation of a pyramidal horn. C_0 is the first waveguide and C_m is the membrane waveguide.

slight misalignment with the $\langle 110 \rangle$ crystal planes, and to variations in the wafer thicknesses from batch to batch.

III. Theory

The theoretical antenna pattern of a single horn-element is calculated assuming an infinite two-dimensional array of horns. It should be noted that we are not calculating the pattern of a phased array, but rather the pattern of a single element in a two-dimensional array. This is because we are interested in a focal-plane array of antennas for multibeam imaging applications. Since the horn dimensions are comparable to a free-space wavelength, the horn-array has to be rigorously analyzed using a complete electromagnetic solution. In this analysis, a horn-element is approximated by a structure of multiple rectangular waveguide sections (Fig. 5), and the fields in each waveguide section are given by a linear combination of waveguide modes. This method has been used

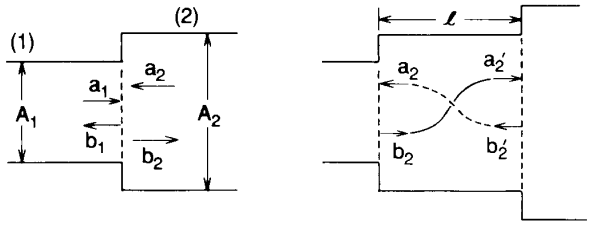

Fig. 6. Forward and backward traveling waves on a waveguide step (left), and a waveguide section (right).

before in the analysis of waveguide transformers [22], and recently applied to the analysis of a corrugated horn [23]. The fields in space are given by two-dimensional Floquet modes [24]. The boundary conditions are matched at each of the waveguide sections, and at the aperture of the horn. The antenna pattern may be calculated by assuming the antenna as either a transmitter or a receiver—the equivalence of these two cases follows from the reciprocity theorem [25]. In our analysis, we assume the horn to be a receiving antenna. The pattern is found by calculating the received fields at the position of an infinitesimal dipole inside the horn, for plane waves incident at different angles. The effect of the membrane on the incident radiation is neglected, since the membrane is very thin compared to a free space wavelength.

A. Pyramidal Horn Characterization

In this section, the scattering matrices of a waveguide-step junction and a linear-waveguide section are derived (Fig. 6). A horn matrix **H** is then calculated, relating the fields in the membrane section C_m to the fields in the opening section C_0. Finally, the Floquet modes in space are matched to the fields in the opening waveguide, and the fields in section C_m are calculated in terms of incident field using the horn matrix **H**.

The transverse fields $(\vec{\mathbf{E}}_t, \vec{\mathbf{H}}_t)$ in waveguide section (1) Fig. (6) can be represented by a linear combination of transverse electric (TE) and (TM) waveguide modes [26],

$$\vec{\mathbf{E}}_t^1 = \sum_{n=0}^{\infty}\sum_{m=0}^{\infty} a_{mn}^{p1} e^{-j(\gamma_{mn}^{p1})z}\,\vec{\mathbf{e}}_{mn}^{p1} + \sum_{n=0}^{\infty}\sum_{m=0}^{\infty} b_{mn}^{p1} e^{+j(\gamma_{mn}^{p1})z}\,\vec{\mathbf{e}}_{mn}^{p1}$$

$$\vec{\mathbf{z}} \times \vec{\mathbf{H}}_t^1 = \sum_{n=0}^{\infty}\sum_{m=0}^{\infty} a_{mn}^{p1} Y_{mn}^{p1} e^{-j(\gamma_{mn}^{p1})z}\,\vec{\mathbf{e}}_{mn}^{p1} - \sum_{n=0}^{\infty}\sum_{m=0}^{\infty} b_{mn}^{p1} Y_{mn}^{p1} e^{+j(\gamma_{mn}^{p1})z}\,\vec{\mathbf{e}}_{mn}^{p1} \quad (1)$$

where p denotes either a TE or a TM mode, γ_{mn}^{p1} is the wave propagation constant and is real for a propagating wave and imaginary for an attenuating wave, Y_{mn}^{p1} is the wave admittance for a TE/TM mode, and $\mathbf{e}_{mn}^{p1}$ is a TE/TM eigenvector normalized such that the power carried by a given wave is proportional to the square of its coefficient (a_{mn}^{p1} or b_{mn}^{p1}). The fields in waveguide section (2) follow the same representation. The coefficients a_{mn}^{p1} and b_{mN}^{p1} are unknown, and will be calculated later in terms of the incident field on the horn array. The boundary conditions at the waveguide-step junc-

tion are the continuity of the transverse electric and magnetic fields over the area A_1, and the vanishing of the transverse electric field on the area $(A_2 - A_1)$. Using the Galerkin mode matching technique [27], we get a set of linear equations

$$\sum_n \sum_m \left(a_{mn}^{p1} + b_{mn}^{p1}\right) V_{mnMN}^{p1p2} = a_{MN}^{p2} + b_{MN}^{p2} - Y_{mn}^{p1}\left(a_{mn}^{p1} - b_{mn}^{p1}\right) = \sum_N \sum_M Y_{MN}^{p2} V_{MNmn}^{p1p2}\left(a_{MN}^{p2} - b_{MN}^{p2}\right) \quad (2)$$

where V_{mnMN}^{p1p2} is the scalar product between a TE/TM eigenvector in waveguide section (1) and a TE/TM eigenvector in waveguide section (2), given by

$$V_{mnMN}^{p1p2} = \int_{A1} \vec{\mathbf{e}}_{mn}^{p1} \cdot \vec{\mathbf{e}}_{MN}^{p2}\, dA_1. \quad (3)$$

The fields in waveguide section (1) can then be related to the fields in waveguide section (2) through the matrix equation

$$\begin{pmatrix} V & V \\ Y_1 & -Y_1 \end{pmatrix}\begin{pmatrix} a_1 \\ b_1 \end{pmatrix} = \begin{pmatrix} I & I \\ -V^T Y_2 & V^T Y_2 \end{pmatrix}\begin{pmatrix} a_2 \\ b_2 \end{pmatrix} \quad (4)$$

where I is a unit matrix, Y_1 and Y_2 are diagonal admittance matrices of the individual TE/TM modes in sections (1) and (2), respectively. V is a scalar-product matrix of the eigenmodes at the interface, and V^T is the transpose of V. (a_1, b_1) and (a_2, b_2) represent the coefficients of the incident and reflected fields for waveguide sections (1) and (2), respectively.

The fields in a lossless-waveguide section (Fig. 6) are related by a simple phase-delay matrix, given by

$$\begin{pmatrix} a_2 \\ b_2 \end{pmatrix} = \begin{pmatrix} 0 & e^{-j(\gamma_{mn})l} \\ e^{+j(\gamma_{mn})l} & 0 \end{pmatrix}\begin{pmatrix} a'_2 \\ b'_2 \end{pmatrix}. \quad (5)$$

The coefficients of the fields in the membrane section C_m can be related to the coefficients of the fields in the first section C_0 by multiplying the step and delay matrices of a large number of waveguide sections together. The resultant matrix is called the horn matrix **H**. The smallest waveguide section C_s is chosen to be small enough to have only rapidly decaying evanescent waves. This section is assumed to be an infinite rectangular waveguide with waves traveling only in the negative z-direction. This is important for the numerical solution because large exponential decay constants are avoided. The boundary condition at C_s relates the forward and backward traveling waves in the waveguide sections. This results in only one independent set of variables at C_0 to match to the incident field.

B. Matching to the Floquet Modes

The transverse fields in air $(\vec{\mathbf{E}}_t^f, \vec{\mathbf{H}}_t^f)$ can be represented by a linear combination of TE and TM Floquet modes [24],

$$\vec{\mathbf{E}}_t^f = a_{00}^{pf} e^{+j(\gamma_{00}^{pf})z}\vec{\mathbf{e}}_{00}^{pf} + \sum_{n=-\infty}^{\infty}\sum_{m=-\infty}^{\infty} b_{mn}^{pf} e^{-j(\gamma_{mn}^{pf})z}\vec{\mathbf{e}}_{mn}^{pf}$$

$$\vec{z} \times \vec{\mathbf{H}}_t^f = -a_{00}^{pf} Y_{00}^{pf} e^{+j(\gamma_{00}^{pf})z}\vec{\mathbf{e}}_{00}^{pf} + \sum_{n=-\infty}^{\infty}\sum_{m=-\infty}^{\infty} b_{mn}^{pf} Y_{mn}^{pf} e^{-j(\gamma_{mn}^{pf})z}\vec{\mathbf{e}}_{mn}^{pf} \quad (6)$$

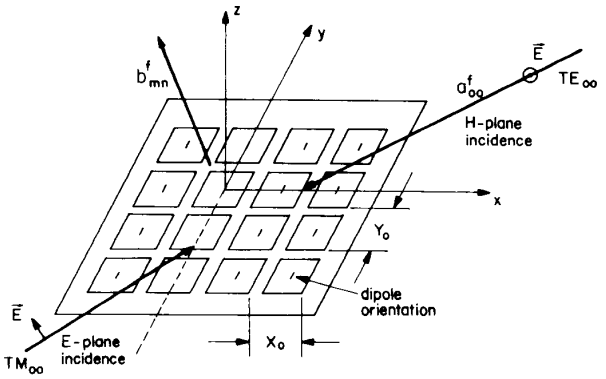

Fig. 7. Incident plane waves for E- and H-plane pattern calculation.

where a_{00}^{pf} and b_{mn}^{pf} are the coefficients of the incident plane wave and the reflected Floquet modes, respectively, and p, γ_{mn}^{pf}, Y_{mn}^{pf} and $\vec{\mathbf{e}}_{mn}^{pf}$ are in the same notation as the fields in waveguide section (1). The orthonormalized set of eigenvectors $\vec{\mathbf{e}}_{mn}^{pf}$ are derived from the potential function of a plane wave incident on a periodic structure.

The same method is used to match the fields in air to the fields in C_0. The coefficients of the fields in waveguide section C_0 can be related to the coefficients of the fields in air through the matrix equation

$$\begin{pmatrix} F & F \\ Y_0 & -Y_0 \end{pmatrix}\begin{pmatrix} a_0 \\ b_0 \end{pmatrix} = \begin{pmatrix} I & I \\ -F^T Y_f & F^T Y_f \end{pmatrix}\begin{pmatrix} a_f \\ b_f \end{pmatrix} \quad (7)$$

where I is a unit matrix, Y_0 and Y_f are diagonal matrices of the individual waveguide and Floquet modes, and (a_0, b_0) and (a_f, b_f) are the coefficients of the incident and reflected fields for C_0 and air, respectively. F is a matrix of the scalar product between a TE/TM eigenvector in waveguide section C_0 and a TE/TM Floquet eigenvectors in air, given by

$$F_{mnMN}^{p1pf} = \int_{A_0} \vec{\mathbf{e}}_{mn}^{p1} \cdot \vec{\mathbf{e}}_{MN}^{pf}\, dA_0. \quad (8)$$

The incident field is a plane wave of unit amplitude and its coefficients a_{00}^{pf} are known. The coefficients of the reflected Floquet modes b_{mn}^{pf}, and the coefficients of the waveguide modes $a_{mn}^{p_0}$ and $b_{mn}^{p_0}$ can be calculated in terms of the coefficients of the incident field. The incident field is a TM_{00} plane wave for the E-plane pattern calculations, and a TE_{00} plane wave for the H-plane pattern (Fig. 7).

The theory developed above is valid for horns with any rectangular cross-section, having an arbitrary separation between the horn apertures. The only condition is that the array is periodic and infinite in extent. The horn was modeled using 50 steps per wavelength, the smallest section C_s being 0.2 λ. In the case of E- and H-plane pattern calculations, only certain waveguide modes are excited because of symmetry. All relevant modes were considered up to $M = N = 7$. The patterns were calculated for square apertures, with the periods of the two-dimensional array, X_0 and Y_0, taken equal to the horn aperture C_0. The separation between the horn openings is neglected, since it is much smaller than C_0.

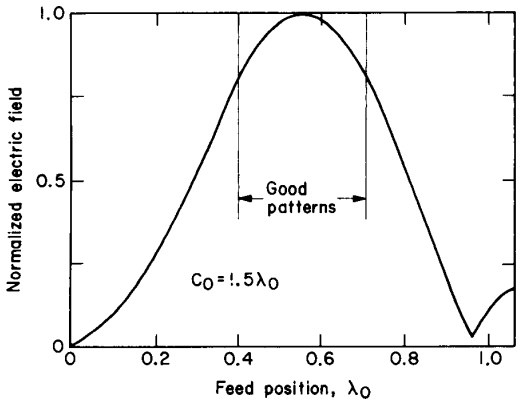

Fig. 8. Normalized fields on the horn axis for a plane wave incident normal to the aperture.

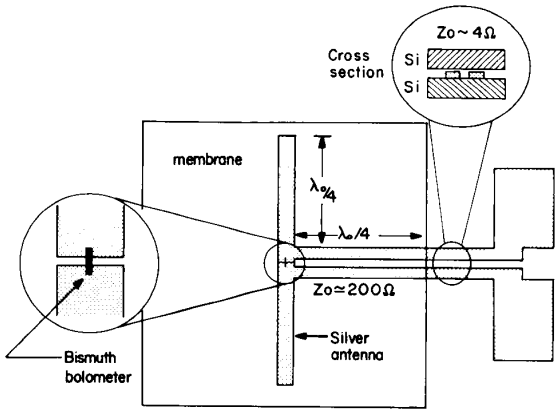

Fig. 9. Quarter-wave dipole with a low-pass filter on the membrane.

The horn sidewalls are assumed to be lossless. The following tests were conducted to check the accuracy of the results:

1) Conservation of power—the sum of power in the reflected modes must equal the power in the incident modes. This is true because an infinitesimal dipole does not absorb any power, and the walls are assumed to be lossless.
2) Boundary conditions—the fields at C_0 calculated from the waveguide-modes representation must match the fields calculated from the Floquet-mode representation.
3) Reciprocity theorem—the coupling between any two Floquet modes must remain the same if the incident and reflected modes are interchanged.

IV. Design of the Horn Structure

The horn structure is designed to produce a desirable radiation pattern for an imaging system. The variable parameters are the dimensions of the horn and the position of the dipole inside the horn. Fig. 8 shows the normalized electric field along the horn axis (starting from the apex) for a plane wave incident normal to a 1.5 λ square horn array. At a feed position smaller than 0.35 λ, the membrane cross section is smaller than 0.5 λ, and the fields decrease uniformly because all the waveguide modes are in the cut-off region. There is also a defocusing effect around a feed position of 0.92 λ. The patterns calculated at feed positions of 0.42 λ, 0.56 λ, and 0.71 λ show good horn patterns, indicating a wide horn-bandwidth. Also, the pattern at 0.42 λ was better than the pattern at 0.56 λ. This shows that the point of maximum field intensity is not necessarily the point which gives the best radiation pattern.

Imaging arrays with square horn apertures of 1.0 λ, 1.45 λ and 2.1 λ were fabricated for 242 GHz, and a 1.0 λ array was fabricated for 93 GHz. In all cases, the feed position was 0.39 λ, and the membrane side length was around 0.55 λ. The probe antennas were λ/4 dipoles with an integrated coplanar-strip isolation filter (Fig. 9). The coplanar strips are designed to have a characteristic impedance of 200 Ω when suspended on the membrane, (calculated from the quasi-static solution to coplanar strips in free space [28]), and an impedance of 4 Ω when sandwiched between two silicon wafers. The quarter-wave section of coplanar strips transforms the 4 Ω impedance into a very large parallel impedance at the dipole apex. The bolometer presents there a much lower impedance, and therefore absorbs all the received power.

V. Measurements

Microwave measurements were made on a 3 × 3 scale aluminum model of the 93 GHz array at around 7.3 GHz to determine the impedance of the dipole probe antenna inside the pyramidal cavity. A coaxial line feeds a dipole antenna and a coplanar-strip transmission line which is shorted λ/4 away from the feed. This design has two purposes. It models the coplanar strips on the membrane effectively, and it provides an effective balun [2] for the coax-dipole feed. The measured impedance, 50 Ω + *j*95 Ω, is highly inductive. The 93-GHz antenna will have an additional series resistance resulting from loss in the metal. The dipole thickness is only about a third of the skin depth, so that we can safely take the RF series resistance to be the same as the dc series resistance, which is approximately 4 Ω. The estimated 93-GHz antenna impedance is thus $Z_a = 54\ \Omega + j95\ \Omega$.

Millimeter-wave measurements were made at 93 GHz and 242 GHz. At 93 GHz, the source was a Varian reflex klystron modulated at 1 kHz with a power output of 80 mW. At 242 GHz, the source was a Millitech waveguide-tripler fed by an 80.7 GHz Gunn diode modulated at 1 kHz. The power output of the tripler was about 1 mW. The detected signal was fed to a lock-in amplifier. Care was taken to reduce scattering from the antenna and source mounts.

Measurements were made in the *E*- and *H*-planes and 45° planes of both the co-polarized and cross-polarized components. Full two-dimensional scans were also made of the co-polarized component. Patterns measurements were made on four different elements within the imaging array. Single element patterns are given here; the results for the other elements are very similar. No measurements were made on elements at the edge of the array.

VI. Patterns: Theory Versus Experiment

The measured patterns at 93 and 242 GHz show good agreement with theory (Figs. 10–15). The *E*-plane pattern of

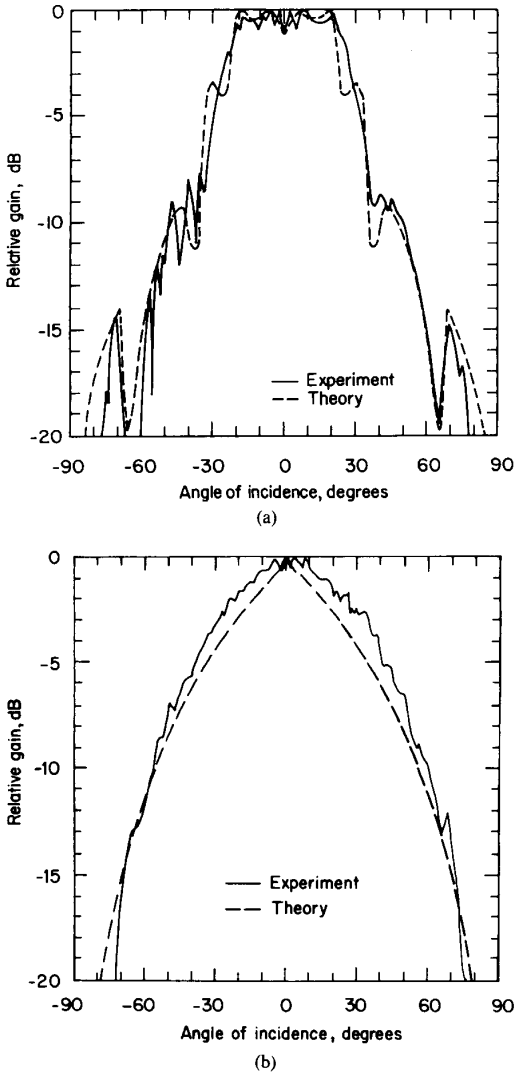

Fig. 10. Typical E-plane (a) and H-plane (b) patterns measured at 93 Ghz on a (7 × 7), 1.0 λ imaging array. Notice the −14 dB sidelobes in the E-plane.

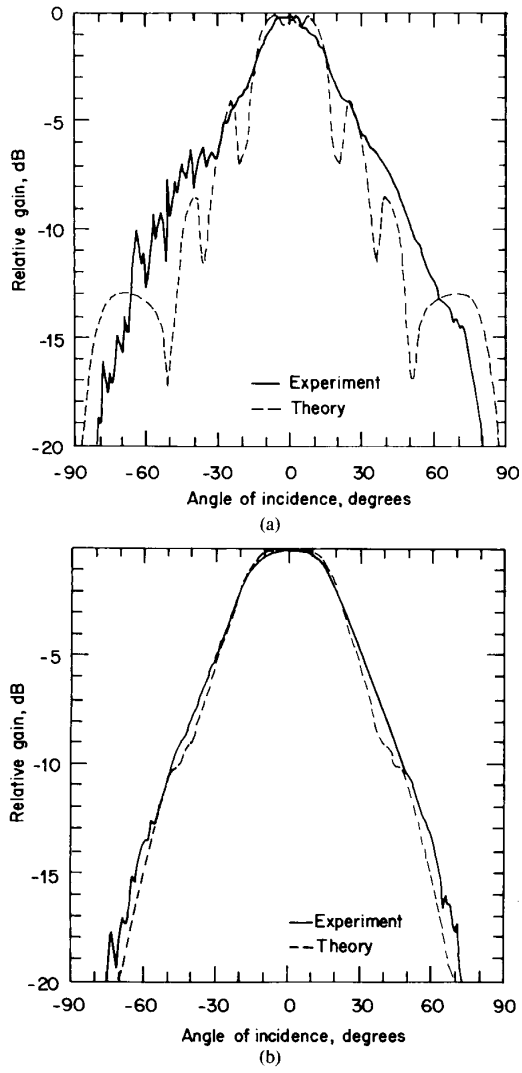

Fig. 11. Typical E-plane (a) and H-plane (b) patterns measured at 242 GHz on a (9 × 9), 1.45 λ imaging array. The zigzags on the measured E-plane pattern are due to scattering from the antenna mount.

the 1.45 λ array measured at 242 GHz does not exhibit any sidelobes. We attribute this to losses in the cavity sidewalls, which were not coated by a gold layer. In contrast, the sidewalls for the 93 GHz array were gold coated, and the E-plane pattern of the 1.0 λ array measured at 93 GHz (Fig. 10) shows slight gain suppression at normal incidence and sidelobes as predicted by the theory. The sidelobes result from the incident energy scattering into successively higher order Floquet modes. A 1.0 λ array was constructed for 242 GHz which did not incorporate gold plating on the horn sidewalls. The measured patterns (not shown) were similar to the 93 GHz 1.0 λ array except for the absence of sidelobes. The discrepancy between theory and experiment in the E-plane pattern of the 2.1 λ arrays (Fig. 12) can also be explained by the large resistive sidewall loss. In this case, the cavity was not gold coated, and the silicon wafer was lightly doped.

The horn antennas were linearly polarized parallel to the probe dipole. The cross-polarized component at normal incidence was limited by the noise floor, which ranged from −20 to −30 dB depending on the quality of the bolometers. There was also no measurable cross-polarized component in either the E- or H-planes. This is due to the symmetrical structure of the antenna. The 45° cross-polarized patterns were symmetrical about normal incidence, and showed a peak cross-polarized component at ±60° (Fig. 13).

Tabulated in Table I are the exact dimensions of the imaging arrays, with the corresponding measured 3- and 10-dB beamwidths of the E- and H-plane patterns. The calculated directivities from the co-polarized two-dimensional scans show a decreasing horn-aperture efficiency with increasing aperture size. From a transmitting point of view, a horn with a large aperture is not uniformly illuminated by the dipole and suffers from aperture taper (nonuniform field

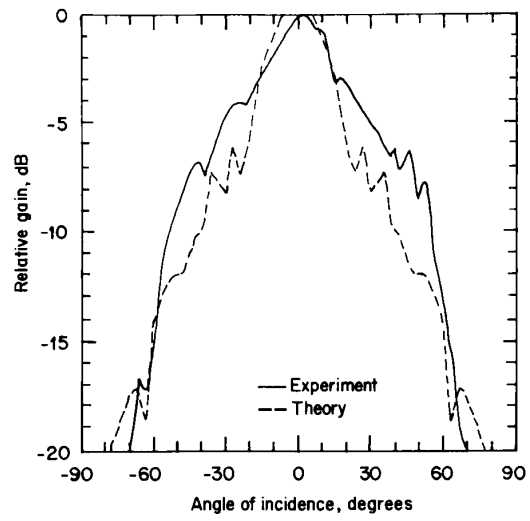

(a)

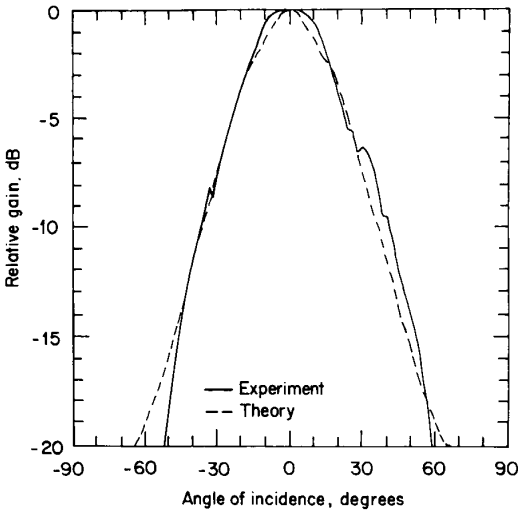

(b)

Fig. 12. Typical E-plane (a) and H-plane (b) patterns measured at 242 GHz on a (7 × 7), 2.1 λ imaging array.

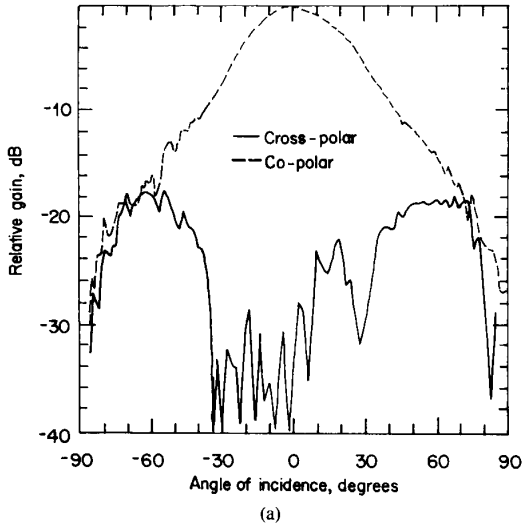

(a)

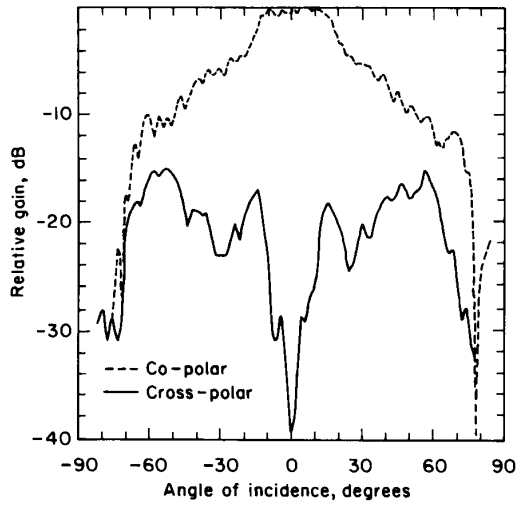

(b)

Fig. 13. Typical 45° co-polar and cross-polar plane patterns measured at 242 GHz on a (9 × 9), 1.45 λ imaging array (a), and at 93 GHz on a (7 × 7), 1.0 λ imaging array (b).

distribution) and phase errors. Also, the H-plane pattern narrows with increasing aperture size, while the E-plane remains the same after 1.45 λ. This is due to the boundary conditions at the horn aperture.

VII. Horn-Aperture Efficiency at 93 GHz

The horn-aperture efficiency of a single element in the array is defined as the power received by the bolometer divided by the total power incident on the horn aperture. To measure this, we must calibrate the bolometer, and measure the gain and the power transmitted from the source. Details of the procedure are given in [20]. The measured horn-aperture efficiency is 44 ± 4%, or −3.6 dB.

It is important to account for the different contributions to the measured loss, because this indicates the potential for improvements. Table II gives the breakdown of the losses. The total calculated losses are 3.4 dB [20]. The largest loss is the 2.2 dB dipole mismatch loss between the probe dipole and the bolometer. It is given by the formula $4R_aR_b/|Z_a + R_b|^2$, where R_a is the antenna radiation resistance (50 Ω), R_b is the bolometer resistance (138 Ω), and Z_a is the antenna impedance (54 + j95 Ω). The next biggest loss is resistive loss in the horn sidewalls, which is equal to 0.7 dB. In this case, the 93 GHz horn array was assembled from four different stacked wafers, and the membrane wafer was not gold coated. It should be possible to reduce the mismatch and wall losses, if all the horn sidewalls are gold coated, and the antenna is matched. The aperture efficiency of a 1.0 λ square horn should then be around 88%.

VIII. System Coupling Efficiency Measurements

The coupling efficiency to an imaging system is defined as the power received by a single element placed at the focal point of an imaging system, divided by the total power

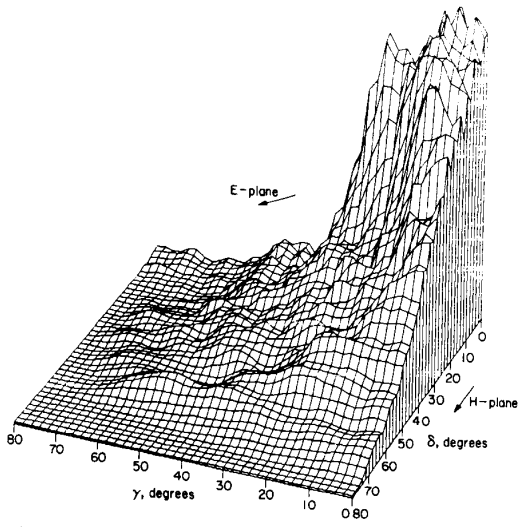

Fig. 14. Measured two-dimensional scans of a (7 × 7) array at 93 GHz. Vertical scale is linear in power.

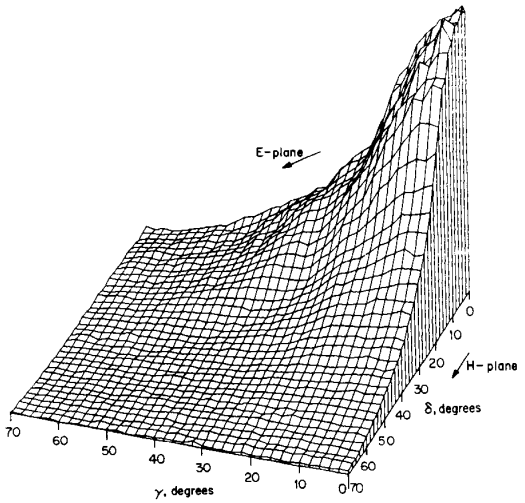

Fig. 15. Measured two-dimensional scans of a (9 × 9) array at 242 Ghz. Vertical scale is linear in power.

TABLE I
MEASURED 3-dB AND 10-dB BEAMWIDTHS OF SEVERAL MILLIMETER-WAVE IMAGING ARRAYS.

Array	1.0 λ	1.45 λ	2.1 λ
f GHz	93	242	242
C_0/λ	1.01	1.42	2.09
Sep./λ	0.02	0.03	0.02
S_{mbr}	25%	13.5%	7.5%
E (3-dB)	54°	35°	35°
E (10-dB)	100°	95°	97°
H (3-dB)	62°	46°	32°
H (10-dB)	110°	90°	70°
D_{cp}	11.9	17.3	21
ϵ_{cp}	95%	67%	38%

"Sep." is the separation between two openings C_0, and S_{mbr} is the percentage of the space on the wafer occupied by the membranes and the antennas.

TABLE II
CALCULATED AND MEASURED HORN APERTURE-EFFICIENCY LOSSES

Intrinsic Pattern Loss	-0.2 dB
Mismatch Loss	-2.2 dB
Horn-Sidewall Loss	-0.7 dB
Cross-Polarization Loss	-0.2 dB
Horn-to-Horn Coupling Loss	-0.1 dB
Total Calculated Loss	-3.4 dB
Total Measured Loss	-3.6 dB

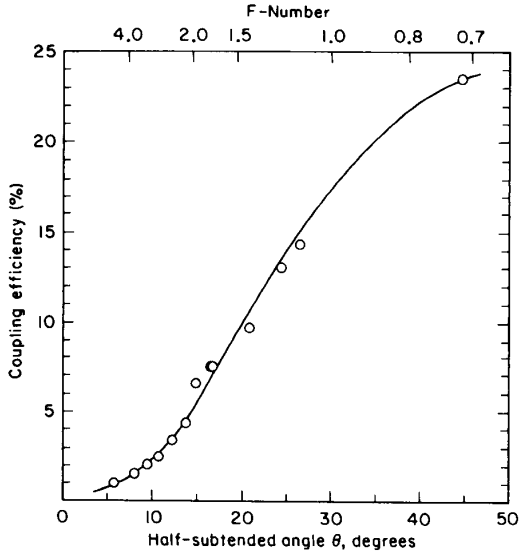

Fig. 16. Coupling efficiency of a horn element in a 1.0 λ imaging array. Measured points, indicated by circles, include the mismatch and resistive losses in the horn element, and the taper and spillover losses of the lens.

incident on the primary lens, when the lens is illuminated by a plane wave. The coupling efficiency of the 1.0 λ imaging array was measured at 93 GHz for systems of different f-number (Fig. 16). These were produced by placing aperture-stops over the lens. We found that 24% of the incident power is absorbed by a single detector for an f-number of 0.7, and 14% for an f-number of 1.1. If matching and sidewall losses were eliminated, the efficiency would be 54%. This agrees with the theoretical coupling-efficiency of 60% [30].

The distribution of power in the focal plane, for an incident plane-wave normal to the lens, was measured for two separate lenses with f-numbers of 1.1 and 0.7, respectively (Fig. 17). The sum of the total power on the focal plane yields a total coupling efficiency of 25% for both lenses. The lens Airy pattern [31] has a first dark-ring radius of 0.61 λ and 1.22 λ for an $f \setminus 0.7$ and $f \setminus 1.1$ lens, respectively. The center element receives 96% of the total power incident on the focal plane for an $f \setminus 0.7$ lens, and 56% for an $f \setminus 1.1$ lens. There is then a strong optical coupling between the elements for an $f \setminus 1.1$ lens, i.e., for a diffraction limited imaging array. Hence, a significant fraction of the power appropriated to the central element is distributed among adjacent elements, and this central element also receives power appropriated to its neighbors. This optical coupling

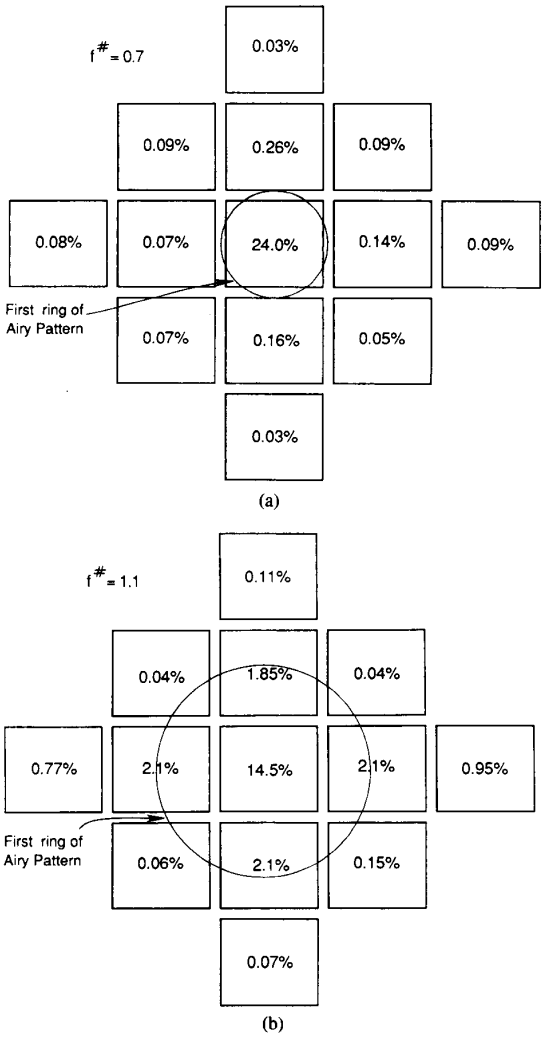

Fig. 17. Distribution of power in the focal plane as a percentage of the total power incident on the lens, for $f \setminus 0.7$ lens (a) and $f \setminus 1.1$ lens (b).

will blur the image, although in principle, the information is recoverable by coherent processing. On the other hand, the optical coupling in a $f \setminus 0.7$ system is negligible, and the coupling efficiency to the central element is much larger. The penalty paid is an undersampling of the image.

IX. Conclusion

A new monolithic millimeter-wave two-dimensional horn imaging array has been presented. This novel configuration allows ample space for low-frequency interconnections, while still maintaining efficient diffraction-limited imaging. The array is analyzed rigorously by approximating the horn antenna by a structure of multiple rectangular waveguide sections. Pattern measurements at 93 and 242 GHz agree well with the theory, and display a centralized peak in the E- and H-plane patterns. The results show that horn antennas with an opening between 1.0 λ and 1.5 λ have high aperture efficiencies and would couple to appropriate imaging systems well. A horn aperture efficiency of 44% ± 4% was measured at 93 GHz on a 1.0 λ imaging array. Microwave modeling at 7.3 GHz indicates that the major loss component is the mismatch loss between the probe dipole and the detector. The other main contribution arises from the horn sidewalls. It should be possible to reduce the mismatch and wall losses, and thus result in a 1.0 λ imaging array with an aperture efficiency around 88%. A system coupling efficiency of 24% has been measured at 93 GHz for a $f/0.7$ imaging system including spillover, taper, mismatch and resistive losses. The distribution of power in the focal plane indicate that the imaging array is well suited for diffraction-limited imaging. Finally, the horn-array could be used as a monolithic phased array, with the power combiners and phase shifters occupying the available space near the antennas.

Acknowledgment

The authors would like to thank Prof. Rick Compton of Cornell University and Prof. Ross McPhedran of Sydney University for helpful discussions. They also thank Dr. Wade Regehr and Kent Potter for technical help. Dr. P. A. Stimson is supported by a CSIRO of Australia Postdoctoral Award.

References

[1] W. J. Wilson, R. J. Howard, A. C. Ibbott, G. S. Parks and W. B. Ricketts, "Millimeter-wave imaging sensor," *IEEE Trans. Microwave Theory Tech.*, vol. MTT-34, pp. 1026-1035, 1986.

[2] J. P. Hollinger, "A versatile millimeter-wave imaging system," *IEEE Trans. Microwave Theory Tech.*, vol. MTT-24, pp. 786-793, 1976.

[3] E. K. Reedy, G. W. Ewell, "Millimeter Radar," in *Infrared and Millimeter Waves*, vol. 4, K. J. Button, Ed. New York: Academic, 1983, pp. 23-94.

[4] P. E. Young, D. P. Neikirk, P. P. Tong, D. B. Rutledge, and N. C. Luhmann, "Multichannel far-infrared imaging for fusion plasmas," *Rev. Sci. Instrum.*, vol. 56, pp. 81-89, 1985.

[5] T. G. Phillips and D. B. Rutledge, "Superconducting tunnel detectors in radio astronomy," *Sci. American*, vol. 254, pp. 96-102, 1986.

[6] C. Zah, D. P. Kasilingam, J. S. Smith, D. B. Rutledge, T. Wang, and S. E. Schwarz, "Millimeter-wave monolithic Schottky diode imaging arrays," *Int. J. Infrared Millimeter Waves*, vol. 6, pp. 981-997, 1985.

[7] D. B. Rutledge and M. S. Muha, "Imaging antenna arrays," *IEEE Trans. Antennas Propagat.*, vol. AP-30, pp. 535-540, July 1982.

[8] D. B. Rutledge, D. P. Neikirk, and D. P. Kasilingam, "Integrated-circuit antennas," in *Infrared and Millimeter Waves*, vol. 10, K. J. Button, Ed. New York: Academic, 1983, pp. 1-90. (Note: The argument k of the elliptic functions of equation (23) should be $\tan^2(45° - \theta/4)$, rather than $\tan(45° - \theta/4)$, where θ refers to the full bow angle.)

[9] R. L. Rogers, D. P. Neikirk, and H. Ling, "Planar matching of antennas on electrically thick dielectric substrates," in *Proc. 12th Int. Conf. Infrared Millimeter Waves*, Lake Buena Vista, Dec. 1987, pp. 288-289.

[10] W. Chu and H. R. Fetterman, "Printed circuit antennas and FET detectors for millimeter-wave imaging," in *Proc. 12th Int. Conf. Infrared Millimeter Waves*, Lake Buena Vista, Dec. 1987, pp. 222-223.

[11] K. S. Yngvesson, D. H. Schaubert, T. L. Korzeniowski, E. L. Kollberg, T. Thungren and J. F. Johansson, "Endfire tapered slot antennas on dielectric substrates," *IEEE Trans. Antennas Propagat.*, vol. AP-33, pp. 1392-1400, Dec. 1985.

[12] R. C. Compton, R. C. McPhedran, Z. Popović, G. M. Rebeiz, P. P. Tong and D. B. Rutledge, "Bow-tie antennas on a dielectric half-space: Theory and experiment," *IEEE Trans. Antennas Propagat.*, vol. AP-35, pp. 622-631, June 1987.

[13] M. N. Afsar, "Dielectric measurements of millimeter-wave materials," *IEEE Trans. Microwave Theory Tech.*, vol. MTT-32, pp. 1598-1609, 1984.

[14] K. Lee and M. Frerking, "Planar antennas on thick dielectric sub-

strates," in *Proc. 12th Int. Conf. Infrared Millimeter Waves*, Lake Buena Vista, Dec. 1987, pp. 216-217.
[15] K. Mizuno, K. Uehara, H. Nishimura, T. Yonekura, and T. Suzuki, "Yagi-Uda array for millimeter-wave imaging," *Electron. Lett.*, submitted.
[16] G. M. Rebeiz, W. G. Regehr, D. B. Rutledge, R. L. Savage, and N. C. Luhmann Jr., "Submillimeter-wave antennas on thin membranes," *Int. J. Infrared Millimeter Waves*, vol. 8, pp. 1249-1256, Oct. 1987.
[17] K. S. Yngvesson, J. F. Johansson, and E. L. Kollberg, "A new integrated slot element feed array for multibeam systems," *IEEE Trans. Antennas Propagat.*, vol. AP-34, pp. 1372-1376, Nov. 1986.
[18] K. E. Peterson, "Silicon as a mechanical material," *Proc. IEEE*, vol. 70, pp. 420-457, May 1982.
[19] D. W. Hess, "Plasma-enhanced CVD: Oxides, nitrides, transition metals, and transition silicides," *J. Vac. Sci. Technol.*, vol. 2, pp. 244-252, Apr.-June 1984.
[20] G. M. Rebeiz, "Monolithic millimeter-wave two-dimensional horn imaging arrays," Ph.D. dissertation, California Inst. Technol., Pasadena, CA, 1988.
[21] D. P. Neikirk, W. W. Lam, and D. B. Rutledge, "Far-infrared microbolometer detectors," *Int. J. Infrared and Millimeter Waves*, vol. 5, pp. 245-278, 1984.
[22] H. Patzelt and F. Arndt, "Double-plane steps in rectangular waveguides and their applications for transformers, irises and filters," *IEEE Trans. Microwave Theory Tech.*, vol. MTT-30, pp. 771-776, May 1982.
[23] J. A. Encinar and J. M. Rebollar, "A hybrid technique for analyzing corrugated and noncorrugated rectangular horns," *IEEE Trans. Antennas Propagat.*, vol. AP-34, pp. 961-968, Sept. 1986.
[24] N. Amitay, V. Galindo, and C. P. Wu, *Theory and Analysis of Phased Array Antennas*. New York: Wiley, 1972, pp. 37-44.
[25] R. S. Elliott, *Antenna Theory and Design*. Englewood Cliffs, NJ: Prentice-Hall, 1981, pp. 41-46.
[26] R. F. Harrington, *Time-Harmonic Electromagnetic Fields*. New York: McGraw-Hill, 1961.
[27] ——, *Fields Computation by the Methods of Moments*. New York: MacMillan, 1968.
[28] K. C. Gupta, R. Garg, and I. J. Bahl, *Microstrip Lines and Slotlines*. Dedham, MA: Artech House, 1979, pp. 195-213.
[29] O. M. Woodward, Jr., "Balance measurements on Balun transformers," *Electron.*, vol. 26, pp. 188-191, Sept. 1953.
[30] D. P. Kasilingam, "Topics in millimeter-wave imaging arrays," Ph.D. dissertation, California Inst. Technol., Pasadena, CA, June 1987.
[31] E. Hecht and A. Zajec, *Optics*. Reading, MA: Addison-Wesley, 1979, ch. 10.

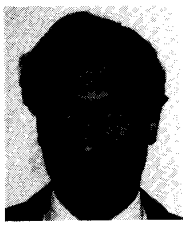

Dayalan P. Kasilingam (S'86-M'86) was born in Colombo, Sri Lanka, on October 24, 1959. He received the B.A. degree in electrical sciences from the University of Cambridge, England, in 1981, and the M.S. and Ph.D. degrees in electrical engineering from the California Institute of Technology, Pasadena, in 1982 and 1987, respectively.

While at Caltech he was a Teaching Assistant in electromagnetic engineering. He joined Ocean Research and Engineering, Pasadena, CA, in December 1986 and has been working on microwave remote sensing of the ocean. His research interests are synthetic aperture radar, radar backscatter from the ocean, polarimetry, adaptive signal processing and stereophotography.

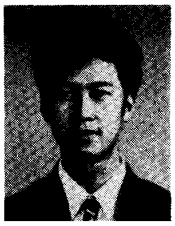

Yong Guo was born in Xian, China, on September 1, 1960. He received the B.S. degree in semiconductor physics from Xian Jiaotong University, Xian, China, in 1982, and the M.S. degree from the California Institute of Technology, Pasadena, in 1987.

He worked at Nanjing Electronic Devices Research Institute, Nanjing, China until 1986. He is currently doing graduate work leading to his Ph.D. degree in electrical engineering at the California Institute of Technology. His interests include millimeter-wave technology and semiconductor devices.

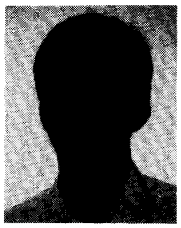

Philip A. Stimson was born in Armidale, Australia, in 1959. He received the B.Sc. (Hons.) degree from the University of New England, Australia, in 1981 and the Ph.D. degree in physics from the University of Sydney, Australia, in 1987.

He has worked at the Australian National Measurement Laboratory (1987), the California Institute of Technology (1988-1989) and is currently at the Jet Propulsion Laboratory, Pasadena, CA. His interests include millimeter-wave technology, lasers and microfabrication of components for these devices.

Gabriel M. Rebeiz (S'86-M'88) was born in Beirut, Lebanon, in 1964. He received the B.E. degree in electrical engineering with distinction from the American University of Beirut in 1982, and the Ph.D. degree in electrical engineering from the California Institute of Technology, Pasadena, in 1988.

He joined the University of Michigan, Ann Arbor, in September 1988 as an Assistant Professor in Electrical Engineering and Computer Science. He has worked on the design, fabrication and measurement of microwave and millimeter-wave antennas, circuits and devices. He developed a wideband log-periodic antenna (100-1500 GHz) on thin silicon-oxynitride membranes, invented a new monolithic two-dimensional horn array (94 GHz, 240 GHz) for efficient diffraction-limited millimeter-wave imaging, and designed and tested large-area bolometers for absolute power calibration at millimeter and submillimeter wavelengths. He is currently establishing the Terahertz Integrated Circuits and Systems (TICS) group at the University of Michigan with research interests in millimeter-wave and submillimeter-wave integrated antennas, radiometers, and phased-arrays.

David B. Rutledge (M'75-S'77-M'77-S'78-M'80-SM'89) was born in Savannah, GA, on January 12, 1952. He received the B.A. degree in mathematics from Williams College, Williamstown, MA, in 1973, the M.A. degree in electrical sciences from Cambridge University, Cambridge, England, in 1975, and the Ph.D. degree in electrical engineering from the University of California, Berkeley, in 1980.

In 1980 he joined the faculty at the California Institute of Technology, Pasadena, where he is now Professor of Electrical Engineering. His research is in developing millimeter and submillimeter-wave monolithic integrated circuits and applications, and in software for computer-aided design and measurement. He is co-author with Professor Richard Compton of Cornell University of the software CAD program, *Puff*, which has over 6000 users worldwide.